metals

MDPI

Article

Study of the Effect of Diamond Nanoparticles on the Structure and Mechanical Properties of the Medical Mg–Ca–Zn Magnesium Alloy

Anton P. Khrustalyov *, Anastasia Akhmadieva, Alexander N. Monogenov, Ilya A. Zhukov, Ekaterina S. Marchenko and Alexander B. Vorozhtsov

Faculty of Physics and Engineering, National Research Tomsk State University, 36 Lenin Ave., 634050 Tomsk, Russia; nas99.9@yandex.ru (A.A.); monogenov@mail.ru (A.N.M.); gofra930@gmail.com (I.A.Z.); 89138641814@mail.ru (E.S.M.); abv1953@mail.ru (A.B.V.)

* Correspondence: tofik0014@gmail.com

Abstract: The paper addresses the production and investigation of the Mg–Ca–Zn alloy dispersion-hardened by diamond nanoparticles. Structural studies have shown that diamond nanoparticles have a modifying effect and make it possible to reduce the average grain size of the magnesium alloy. Reduction of the grain size and introduction of particles into the magnesium matrix increased the yield strength, tensile strength, and ductility of the magnesium alloy as compared to the original alloy after vibration and ultrasonic treatment. The magnesium alloy containing diamond nanoparticles showed the most uniform fracture due to a more uniform deformation of the alloy with particles, which simultaneously increased its strength and ductility.

Keywords: magnesium alloy; nanodiamond particles; structure; dispersion hardening; mechanical properties; fracture

Citation: Khrustalyov, A.P.; Akhmadieva, A.; Monogenov, A.N.; Zhukov, I.A.; Marchenko, E.S.; Vorozhtsov, A.B. Study of the Effect of Diamond Nanoparticles on the Structure and Mechanical Properties of the Medical Mg–Ca–Zn Magnesium Alloy. *Metals* **2022**, *12*, 206. https://doi.org/10.3390/met12020206

Academic Editor: Daolun Chen

Received: 6 January 2022
Accepted: 19 January 2022
Published: 22 January 2022

1. Introduction

Magnesium-based alloys are promising materials for orthopedic implant manufacturing due to a combination of mechanical properties and the grafting ability [1,2]. Moreover, virtually all currently produced magnesium alloys are intended for the automotive and aerospace industries [3,4]. Magnesium is a biodegradable element, and it is sufficiently biocompatible due to its mechanical properties (Young's modulus 41–45 GPa) and density (1.78 g/cm^3) close to human bone [5–7]. Implants made from magnesium-based alloys are supposed to stimulate healing due to the presence of magnesium in human bone tissues [8,9]. Metal implants are typically made from stainless steel, titanium and its alloys, as well as cobalt-chromium alloys, which can adversely affect biocompatibility due to their high wear resistance and high mechanical properties [1,10]. The use of implants made from these alloys implies a prolonged healing of the bone tissue, an increased load on bones with lower mechanical characteristics, and in addition, a second operation is required to remove them from the body [11–13]. The use of magnesium alloys will prevent repeated surgical intervention and minimize the difference in Young's modulus of the bone and implant [6].

Despite all the described advantages, magnesium is not used in medicine due to its insufficient ductility at room temperature [14,15]. Another significant drawback is a high rate of corrosion in the physiological environment, which causes rapid biodegradation with the release of gaseous hydrogen [1,16], and this provides the formation of defects in the form of pores in implants. Mechanical characteristics of magnesium alloys are higher in comparison with pure magnesium, but their corrosion rate is higher due to the presence of secondary phases that promote microgalvanic corrosion [17,18]. Thus, magnesium matrices and secondary phases are galvanic cells, and this requires modification of the alloy microstructure to control the corrosion rate. A ternary system alloy can improve mechanical

properties and increase corrosion resistance. Zinc and calcium, which are found in the human body, are among the most suitable elements. In addition, various coatings applied to a metal implant are used to control alloy corrosion and improve biocompatibility [19–21].

Both the strength of the alloy and the number of secondary phases increase when the calcium content increases, but the ductility decreases [14,16]. Some studies report that introduction of a small amount of nanoparticles increases strength and ductility [22]. A soft metallic matrix can be strengthened using non-metallic particles of oxides, borides, nitrides and other compounds [23,24].

Nanodiamond (ND) is the most biocompatible material among all known carbon nanomaterials [25]. In vitro and in vivo studies showed good biocompatibility of ND, which causes minimal cell cytotoxicity [25–29]. High mechanical properties (hardness, strength) of diamond allow for use of its nanoparticles as effective strengtheners of the metal matrix, a small amount of which increases alloy characteristics [30]. To introduce nanoparticles into a metal matrix, it is possible to use mold casting [31], squeeze casting [32], infiltration [33], and powder metallurgy methods [34]. Despite the advantages of other methods that make it possible to obtain high-density materials and avoid magnesium oxidation, casting into mold is the most universal method, since it allows you to control the distribution of nanoparticles, avoiding their agglomeration and flotation [31,35,36] due to the use of external fields for the melt [35,37].

In this study, ND was used as a hardener for the Mg–Ca–Zn magnesium alloy, and various methods of external effects on the metal melt were employed for their introduction. The study aimed to investigate the ND effect and external effects on the structure, mechanical properties and fracture of the Mg–Ca–Zn magnesium alloy.

2. Materials and Methods

2.1. Material Production

Pure magnesium (99.5 wt % Mg, SOMZ, Solikamsk, Russia), metallic zinc (99.5 wt % Zn, Ural plant of Chemical Products, Verhnaya Pyshma, Russia) and calcium (99.9 wt % Ca, Ural plant of chemical products, Verhnaya Pyshma, Russia), and ND obtained by detonation synthesis were used as starting materials [38]. ND was mixed with magnesium micropowder in ethyl alcohol for 20 min using an ultrasonic bath to obtain a powder mixture Mg-5 wt % ND. Shock-wave compaction was used to obtain a master alloy from the as-prepared powder mixture [39].

To obtain a magnesium alloy, the initial amount of materials was: Mg—99.5 wt %, Ca—1 wt %, Zn—4 wt %. Pure magnesium in the amount of 2000 g was placed in a steel ladle and melted with argon supplied as a protective medium. The alloy was melted using an open-type muffle furnace for easy access and the possibility to process the melt. Argon blowing was performed throughout the entire process of melt treatment prior to pouring it into the casting mold. At a melt temperature of 720 °C, zinc (4 wt %) was introduced using a mechanical mixer [40] at a rotation speed of 1200 rpm until complete dissolution. After that, the melt was held until a temperature of 720 °C was attained, and a steel bell [41] was used to add calcium (1 wt %) to the magnesium with subsequent processing with a mechanical mixer for 20 s. The Mg-5 wt % ND master alloy was introduced into the Mg–Ca–Zn (0.2 wt % ND) melt at 710 °C using a mechanical mixer for 1 min until the master alloy was completely dissolved in the alloy. After the introduction of the master alloy, the melt was poured into a steel casting mold with a working area height of 200 mm, a width of 100 mm, and a thickness of 10 mm. Pouring and solidification of the melt was followed by simultaneous vibration treatment using a vibration stand with a rigidly attached steel chill mold. Vibration treatment of the melt was carried out with a frequency of 60 Hz and amplitude of 0.5 mm. A casting process was used to obtain the Mg–Ca–Zn–ND alloy. The initial Mg–Ca–Zn alloy was obtained with similar parameters without introducing the master alloy. For a comparative assessment of the effect of nanoparticles and external effects, the Mg–Ca–Zn alloy with similar parameters was obtained, but after the introduction of calcium, the melt was subjected to ultrasonic treatment (US). Before ultrasonic treatment,

the waveguide was heated with a melt of commercially pure aluminum to the operating temperature. Ultrasonic treatment was performed using a magnetostrictive water-cooled transducer with a power of 4.1 kV and a frequency of 17.6 kHz for 1 min. Thus, three alloys were obtained: (1) initial Mg–Ca–Zn alloy using vibration treatment; (2) Mg–Ca–Zn–ND alloy containing diamond nanoparticles obtained using vibration treatment; (3) Mg–Ca–Zn US alloy using ultrasonic and vibration treatment. After casting, all alloys were heat treated at a temperature of 300 °C for 6 h, followed by cooling in a furnace.

2.2. Research Methods

The initial diamond nanoparticles were examined by transmission electron microscopy using a Philips CM 30 microscope. The elemental composition of the alloys was studied using a Shimadzu XRF-1800 sequential X-ray fluorescence spectrometer (Shimadzu, Tsukinowa, Japan). Phase analysis of the alloys was performed using a Shimadzu XRD 6000 X-ray diffractometer (Shimadzu, Tsukinowa, Japan) with filtered CuKa radiation at diffraction angles from 20° to 80° with 0.1° step and an exposure time of 10 s. Metallographic analysis was performed using an Olympus GX71 (Olympus Scientific Solutions Americas, Waltham, MA, USA) optical microscope and a Tescan Vega II LMU scanning electron microscope (TESCAN ORSAY HOLDING, Brno, Czech Republic). The structure of the cast materials was studied after mechanical grinding, polishing, and etching of picric acid. The average grain size was determined by the secant method in accordance with ASTM 112-13 standard based on the results of at least 300 measurements for each state. For the calculation, at least four images of the structure of the alloy of each composition at various magnifications were used. The porosity of the alloys was estimated using the Archimedes' principle, and the pore size was calculated from microstructure images, similar to the average grain size.

Brinell Hardness (HB) measurements were performed in accordance with ASTM E103. For the experiment, a Metolab 703 hardness tester (Metolab Company, Moscow, Russia) was used. A spherical indenter with a radius of 2.5 mm was used with a force of 62.5 kg and an exposure time of 30 s, and the size of the indentations was controlled within the range of 0.2 D < d < 0.6 D. The surfaces to be examined were prepared using mechanical grinding. For each alloy composition, 10 hardness measurements were carried out in different parts of the alloy in the longitudinal and transverse directions. Compression experiments were conducted using an Instron 3369 universal electromechanical test bench (Instron European Headquarters, High Wycombe, UK). The loading rate was chosen experimentally in the range from 1.2 to 4.8 mm/min. Taking into account that the deformation pattern did not change, the diagrams obtained at a loading rate of 4.8 mm/min were used for the experiments. Samples 9 mm wide, 9 mm long and 20 mm high were cut from the castings by electrical discharge cutting. The test results were obtained in the form of "stress-strain" diagrams, which were used to obtain the values of the yield strength, ultimate strength and ductilities. For each alloy composition, 5 experiments were carried out on the compression of samples cut from different parts of the casting in the longitudinal and transverse directions. Factographic studies of the sample fractures after compression tests of the studied alloys were performed using a Tescan Vega 3 scanning electron microscope (TESCAN ORSAY HOLDING, Brno, Czech Republic).

3. Results and Discussion

Figure 1 shows a TEM image of ND obtained by detonation synthesis. ND nanoparticles are of a regular spherical shape (Figure 1a), and their structure corresponds to that in previous studies of strengthening of aluminum and magnesium based alloys [42]. The average size of diamond nanoparticles calculated using the random secant method (see Section 2.2) was 7 nm (Figure 1b).

Table 1 shows the data of the chemical analysis of magnesium alloys. As a result of casting, the achieved magnesium content was about 94 wt % in all the alloys. The content of zinc and calcium varied depending on the alloy. In the initial Mg–Ca–Zn alloy, the achieved content of zinc and calcium was 4 and 1 wt %, respectively. Casting of the alloy with ND

increased the content of zinc and calcium up to 4.7 and 1.3 wt %, respectively, due to the lower loss of alloying elements during their introduction into the melt.

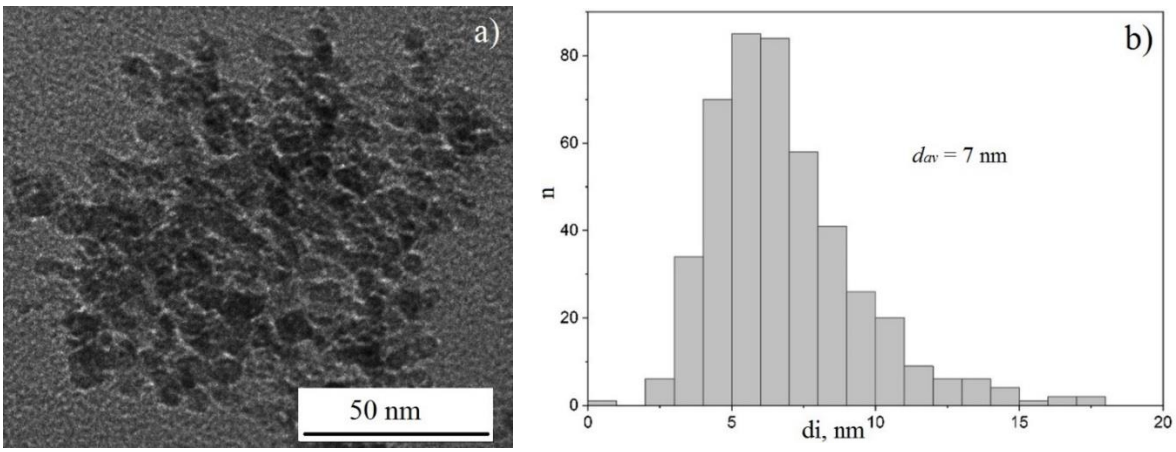

Figure 1. TEM image (**a**) and histogram of particle size distribution (**b**) in the ND powder.

Table 1. Chemical composition (wt %) of the obtained alloys.

Alloy	Mg	Zn	Ca	Si	Al	Fe
Mg–Ca–Zn reference	94.7 ± 0.06	4 ± 0.07	1 ± 0.02	0.12 ± 0.01	0.04 ± 0.01	0.03 ± 0.01
Mg–Ca–Zn–ND	93.6 ± 0.05	4.7 ± 0.07	1.3 ± 0.04	0.17 ± 0.04	0.02 ± 0.01	0.02 ± 0.01
Mg–Ca–Zn US	94.9 ± 0.06	4.2 ± 0.05	0.46 ± 0.03	0.16 ± 0.03	0.1 ± 0.02	0.04 ± 0.02

Ultrasonic treatment of the melt led to the loss of a larger amount of calcium, and its content in the alloy decreased to 0.46 wt %. In addition, heating of the ultrasonic waveguide by the aluminum melt increased the content of aluminum in the alloy, a harmful impurity for biocompatibility of the magnesium implant. The presence of aluminum is due to the need to warm up the ultrasonic wave-water to the operating temperature, which was carried out using an aluminum melt with subsequent cleaning.

Figure 2a shows that the initial alloy contains pores 50 μm in size. In this case, the alloy porosity does not exceed 5 vol %. The introduced ND decreased the alloy porosity up to 3 vol % and pores with a size of up to 15 μm were formed on the surface (Figure 2c), which can be due to the ability of carbon materials to absorb gases dissolved in the melt [43]. This is due to the peculiarities of the production of ND, in which traces of amorphous carbon remain [39]. Thus, the introduction of ND helps to reduce porosity, which will reduce the contact of biological tissues with the material to increase the corrosion resistance of the metal implant. Ultrasonic treatment significantly impairs the cast quality, which surface (Figure 2e) consists of many spherical pores and elongated inhomogeneities. Ultrasonic treatment improves the cast quality [44] and protects the melt with argon; however, an additional volume of gases is captured during melt mixing, which increases the alloy porosity up to 9 vol % and causes defects up to 400 μm long (Figure 2e).

The grain structure of the initial Mg–Ca–Zn alloy consists of equiaxed grains of 50–300 μm in size, on average 180 ± 49 μm (Figure 2b). The introduction of ND led to a decrease in the average grain size to 90 ± 17 μm (Figure 2d) and a more uniform grain distribution in the magnesium alloy. This may indicate the introduction of ND into the magnesium alloy, which is able to inhibit grain growth during solidification and is an effective grain refine for magnesium materials [45]. Ultrasonic treatment of the melt decreased the average grain size of the Mg–Ca–Zn alloy from 180 ± 49 to 110 ± 64 μm (Figure 2f), but the grain size varies over a wide range from 3 to 200 μm. A decrease in the average grain size can also be associated with a lower (2 wt %) calcium content, which, according to studies [46], is the most optimal for grinding the grain structure of magnesium. The structure inhomogeneity can be attributed to the magnesium oxidation

during intense ultrasonic melt treatment, which did not allow effective refining of the Mg–Ca–Zn alloy, however, additional structural studies are required to confirm the presence of oxygen. The presence of MgO particles could also contribute to the refinement of the alloy structure [47] Mg–Ca–Zn after ultrasonic processing. However, according to elemental analysis data (Table 1), oxygen was not detected, which indicates an insignificant content of magnesium oxide in the alloy.

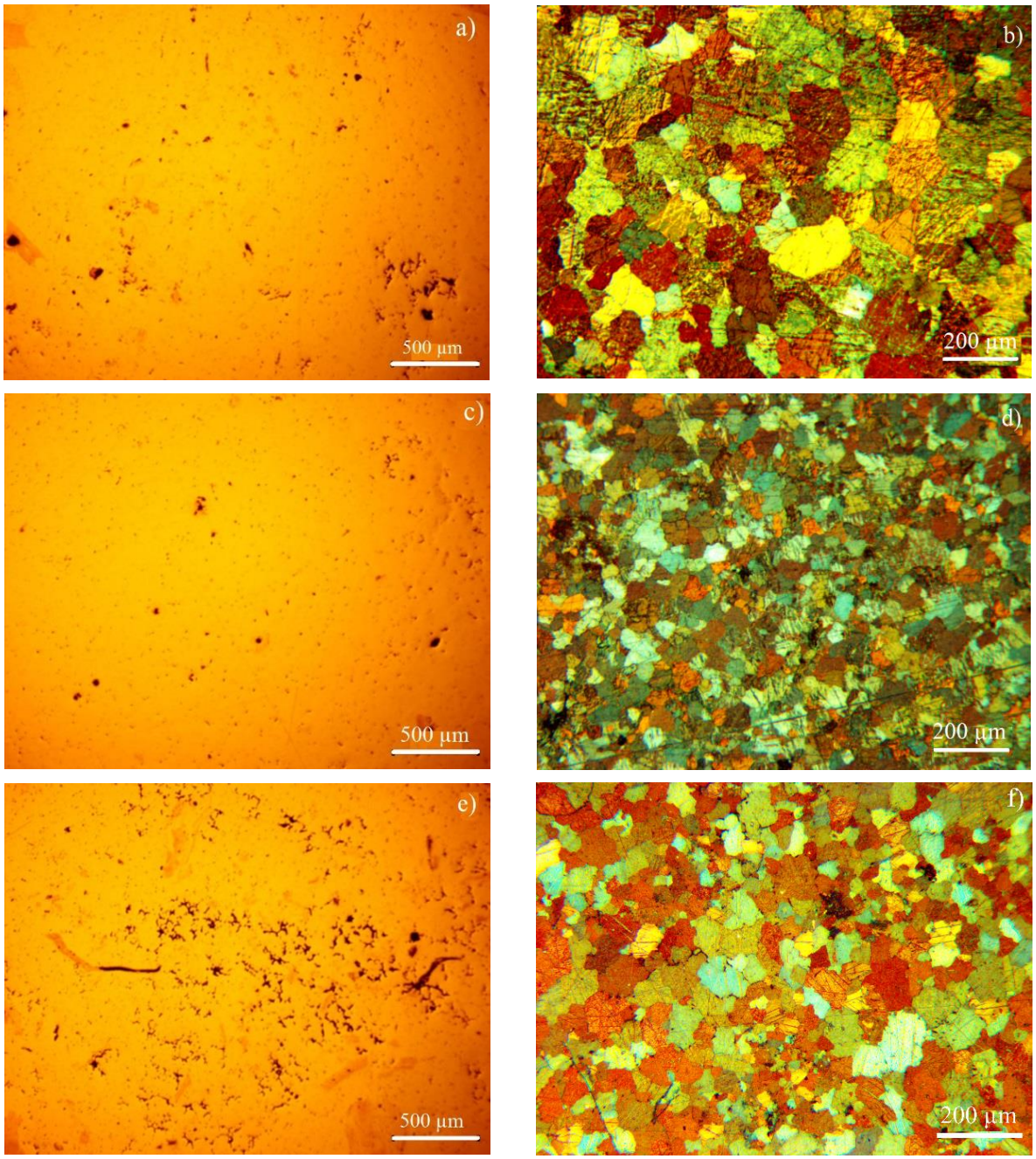

Figure 2. Optical images of magnesium alloys Mg–Ca–Zn reference (**a**,**b**), Mg–Ca–Zn–ND (**c**,**d**) and Mg–Ca–Zn US (**e**,**f**) under natural (**a**,**c**,**e**) and polarized (**b**,**d**,**f**) light.

The alloy microstructure studied by SEM (Figure 3) revealed that the initial Mg–Ca–Zn alloy consists of a matrix (dark area, Figure 3a) and a second phase (light area, Figure 3a) distributed in grain boundaries in the form of a network. The introduction of ND decreased the thickness of the second phase (Figure 3b) through a half-fold reduction of the average grain size of the alloy, which causes ductility of the grain boundary region.

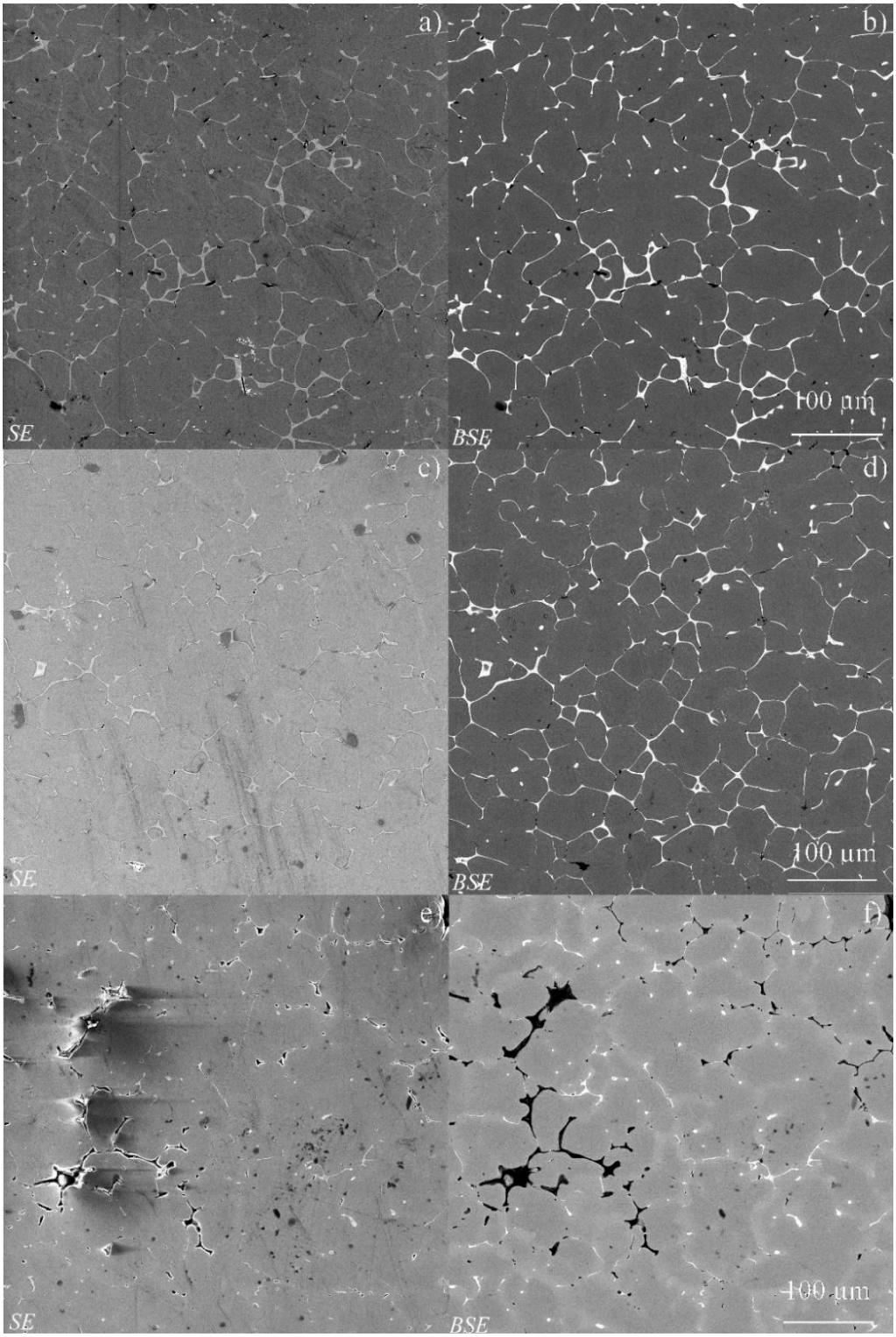

Figure 3. SEM images of the surface of magnesium alloy Mg–Ca–Zn reference (**a**,**b**), Mg–Ca–Zn–ND (**c**,**d**) and Mg–Ca–Zn US (**e**,**f**).

After ultrasonic treatment, the amount of the second phase represented by individual elongated and spherical inclusions in the initial Mg–Ca–Zn alloy reduced significantly (Figure 3c). With regard to the reduced calcium content, the results of chemical analysis (Table 1) suggest that its content significantly affects the formation of the intergranular network of the second phase during heat treatment.

To determine the elemental composition of the second phase in the alloys obtained, a more detailed analysis of the structure was carried out with element mapping (Figure 4). As expected, the alloy consists of a magnesium matrix with inclusions containing calcium and zinc (Figure 4a–c). In the alloy containing ND, carbon-containing regions less than 1 µm in size were found, which may indicate the presence of agglomerates and individual nanodiamond particles in the alloy structure (Figure 4a–c). The alloy Mg–Ca–Zn US consists of a magnesium matrix and inclusions supersaturated with calcium (Figure 4g–i).

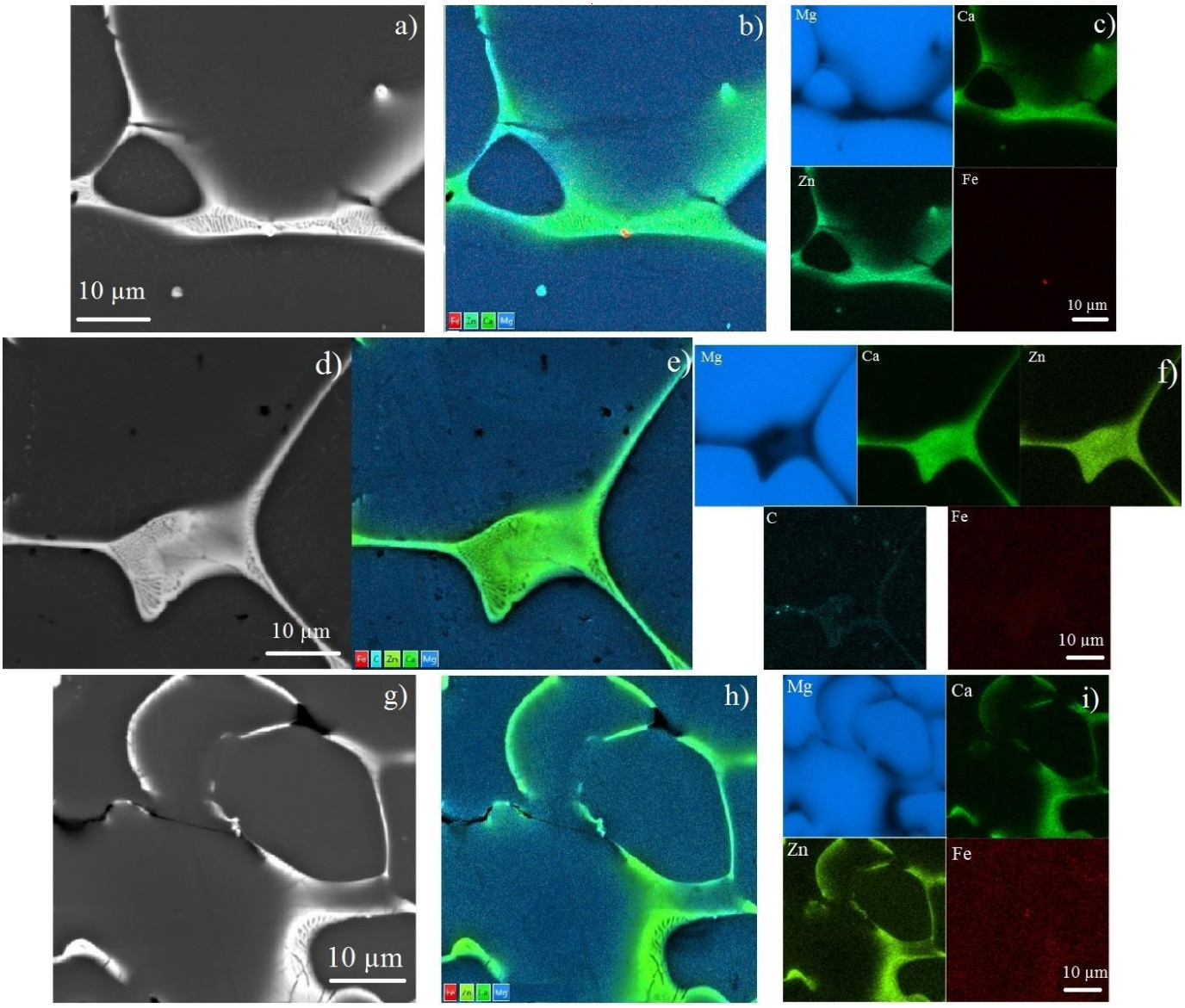

Figure 4. SEM images (**a,d,g**) and results of mapping by elements (**b,c,e,f,h,i**) of magnesium alloys Mg–Ca–Zn reference (**a–c**), Mg–Ca–Zn–ND (**d–f**) and Mg–Ca–Zn US (**g–i**).

According to the results of XRD analysis (Figure 5), the initial alloy contains magnesium and intermetallic $Ca_2Mg_6Zn_3$. The decomposition of a supersaturated solid solution of calcium in magnesium occurs at 160–220 °C [48]. The phase transition Mg + Ca + Zn-> Mg_2Ca + Zn-> $Ca_2Mg_6Zn_3$ occurs at 300 °C with a calcium content of 1 wt % [48].

The Mg–Ca–Zn–ND alloy contains phases of magnesium, and intermetallic compounds $Ca_2Mg_6Zn_3$ and $CaMg_2$. The intermetallic compound $CaMg_2$ is an intermediate phase in the synthesis of $Ca_2Mg_6Zn_3$ in magnesium alloys, and its formation is described in detail in the magnesium-calcium phase diagram [49,50]. The presence of the $CaMg_2$ phase [51] can be attributed to excess calcium due to an insufficient duration of heat treat-

ment, which can attain 48 h [52]. Despite this, the $Ca_2Mg_6Zn_3$ and $CaMg_2$ phases show good biocompatibility, and their presence should not have a negative effect upon further use of the materials obtained [53]. According to the scanning electron data (Figure 4b), the intermetallic phase $CaMg_2$ is distributed along the interdendritic of magnesium. In the Mg–Ca–Zn US alloy, intermetallic phases do not precipitate from Mg-Zn solid solution during alloy heat treatment due to the lower calcium content. Transition from the solid solution to the $Ca_2Mg_6Zn_3$ intermetallic compound requires more than 12 h [54] due to which it is not possible to form the intergranular skeleton (Figure 3e,f) as in the case of alloys Mg–Ca–Zn (Figure 3a,b) and Mg–Ca–Zn–ND (Figure 3c,d). In addition, diffusion of the phase transition can be limited due to a high content of defects in the magnesium alloy structure (Figure 3e,f).

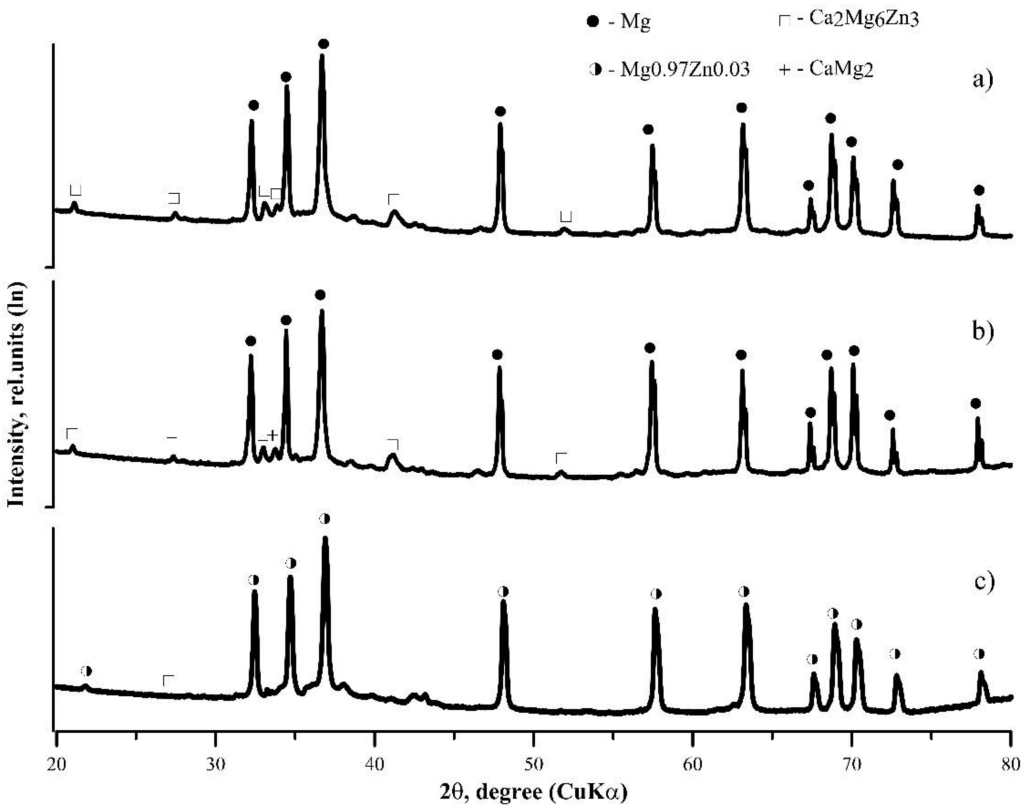

Figure 5. XRD patterns of magnesium alloys Mg–Ca–Zn reference (**a**), Mg–Ca–Zn–ND (**b**) and Mg–Ca–Zn US (**c**).

Figure 6 and Table 2 show the loading diagrams and mechanical properties of the magnesium alloys after compression tests. All alloys exhibit a sufficiently high hardness, which is twofold higher than that of pure magnesium [55]. Table 2 shows that the alloy hardness does not change; however, the data obtained after mechanical compression tests show that the introduction of ND increases the yield v strength of the alloy from 66 to 75 MPa, the ultimate strength from 294 to 332 MPa, and the ductility from 22% to 27%.

Table 2. Mechanical properties of the obtained magnesium alloys.

Alloy	Hardness, HB	$\sigma_{0.2}$, MPa	σ_B, MPa	δ, %
Mg–Ca–Zn reference	54 ± 3	66 ± 2	294 ± 9	22 ± 5
Mg–Ca–Zn–ND	52 ± 2	75 ± 2	332 ± 4	27 ± 0.9
Mg–Ca–Zn US	52 ± 6	63 ± 8	322 ± 12	25 ± 0.5

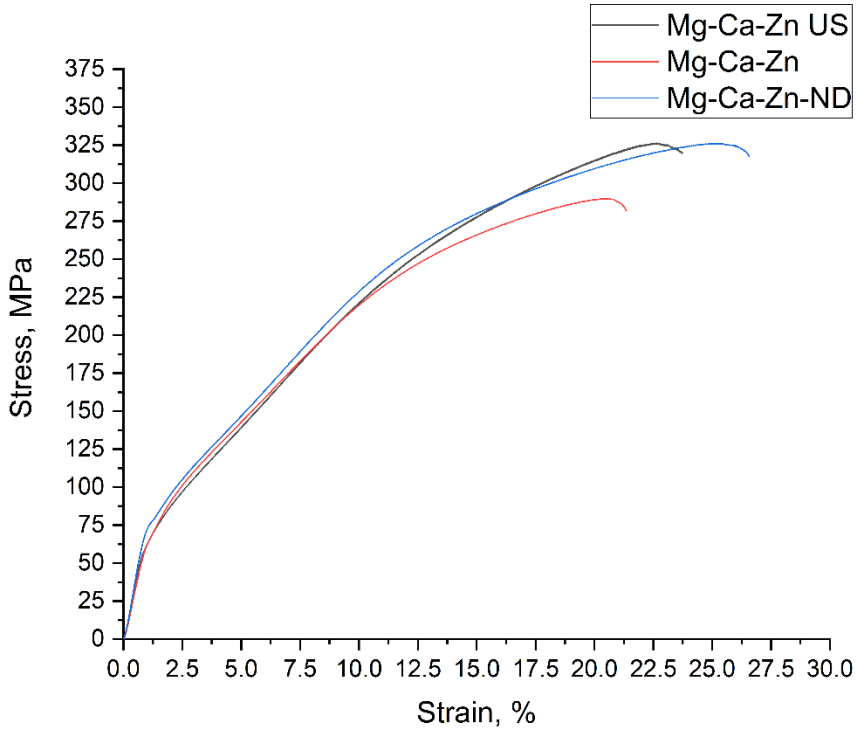

Figure 6. Diagrams of compression tests of magnesium alloys Mg–Ca–Zn.

Despite the increase in the mechanical properties of the Mg–Ca–Zn alloy after the introduction of ND, there is no increase in hardness, which may be due to the low volume content of hardening particles, which is ~0.001 vol % and does not allow one to detect a change in hardness due to the small volume of the deformed material. High hardness of magnesium alloy after ultrasonic treatment (52 HB) can be provided by grain refinement and the presence of intermetallic phases. Apparently, a small scanning area of the XRD analysis does not allow identification of these phases, which ensure an increased alloy hardness. The increased yield strength of the Mg–Ca–Zn alloy can be due to the alloy grain refinement (Figure 4d,e) according to the Hall–Petch law, which directly affects an increase in the yield strength [56–58]. After ultrasonic treatment of the melt, the average grain size reduced (Figure 3f); however, the yield strength of the alloy decreased due to the inhomogeneity of the grain size distribution, the average size of which varies from 3 to 200 μm. A simultaneous increase in the tensile strength and ductility of the magnesium alloy can be attributed to a more uniform deformation of the material as a result of the ND introduction, as it was shown earlier for other nanoparticles in magnesium [59,60] and aluminum [61] alloys. Table 2 shows that the mechanical properties of Mg–Ca–Zn are rather inhomogeneous in the ingot volume and vary in a wide range. A number of samples show sufficiently high mechanical characteristics, some of which increase as compared to the initial alloy. A decrease in the yield strength from 66 to 63 MPa with a simultaneous increase in the ultimate strength from 294 to 322 MPa, and ductility from 22 to 25 %, which may be associated with a lower content of intergranular inclusions that reduce the alloy brittleness, but structural defects do not allow for maximum mechanical properties of the magnesium matrix.

The study of the samples after testing showed a fairly uniform fracture of the initial Mg–Ca–Zn alloy, and cracks are found on the surface after brittle fracture (Figure 7a,b) as a result of stress concentration in the region of structural defects in the alloy. The number of such defects in the ND-containing alloy is significantly reduced, and the fracture surface exhibits significant changes in the fracture plane (Figure 7c,d). This may indicate the effect of nanoparticles on a simultaneous increase in the tensile strength and ductility of the

magnesium alloy (Table 2, Figure 6), which can change the direction of a potential crack in the grain body [61].

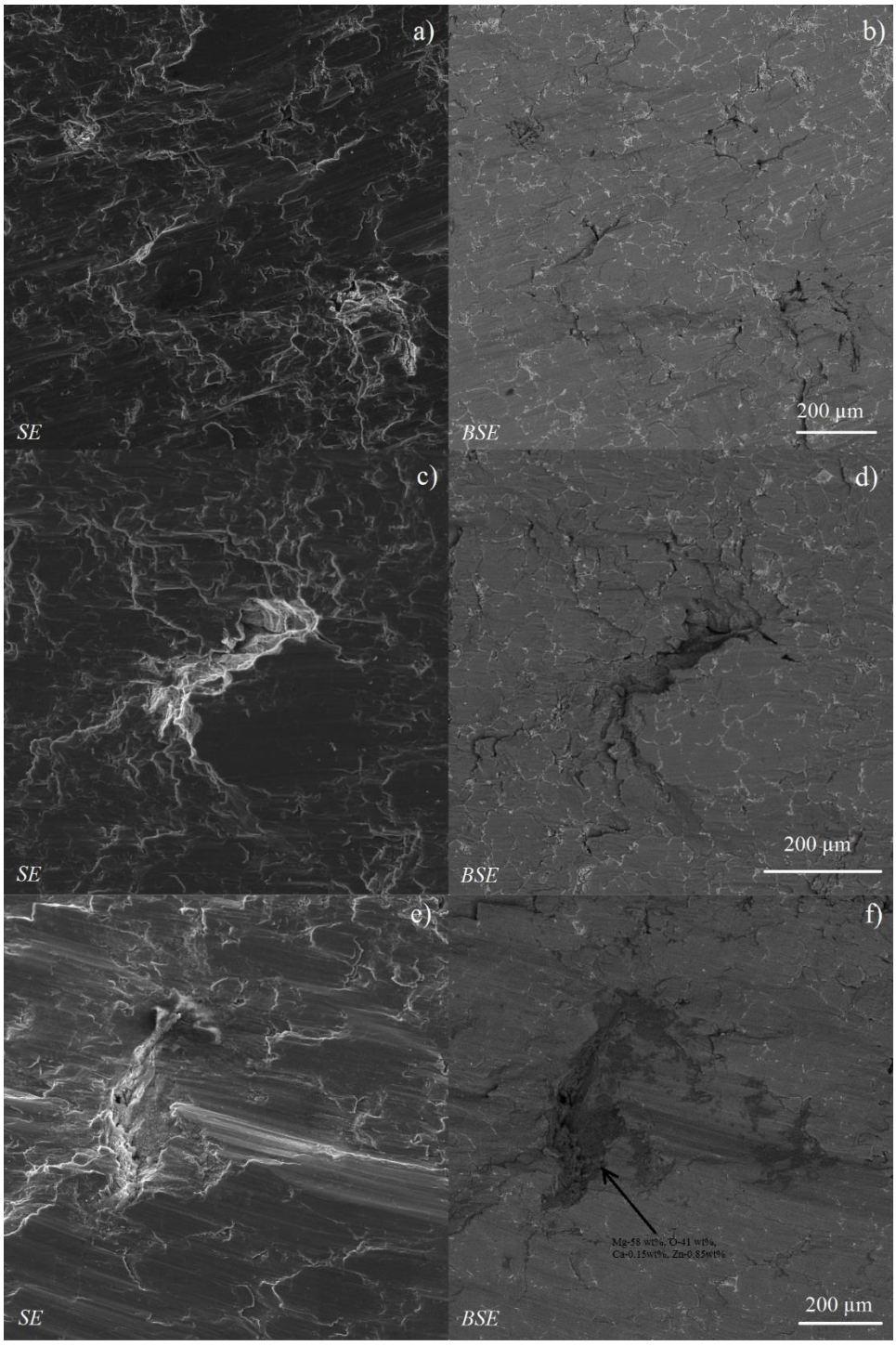

Figure 7. SEM image of the fracture surface of magnesium alloys Mg–Ca–Zn reference (**a**,**b**), Mg–Ca–Zn–ND (**c**,**d**), and Mg–Ca–Zn US (**e**,**f**).

The fracture surface of the Mg–Ca–Zn US alloy shows defects, which hinder attaining the maximum properties of the magnesium matrix (Figure 7e,f). According to the EDS analysis, the dark area contains a large amount of oxygen, which confirms the intense oxidation of the magnesium melt during the ultrasonic treatment, which prevents the effective grinding of the magnesium alloy grain (Figure 2f). A detailed study of the

fracture surfaces (Figure 8) revealed some features of the fracture surface of magnesium alloys after compression. The initial alloy contains inclusions oversaturated with oxygen, which apparently consist of αCa (Figure 5a) that is intensely oxidized when interacting with oxygen.

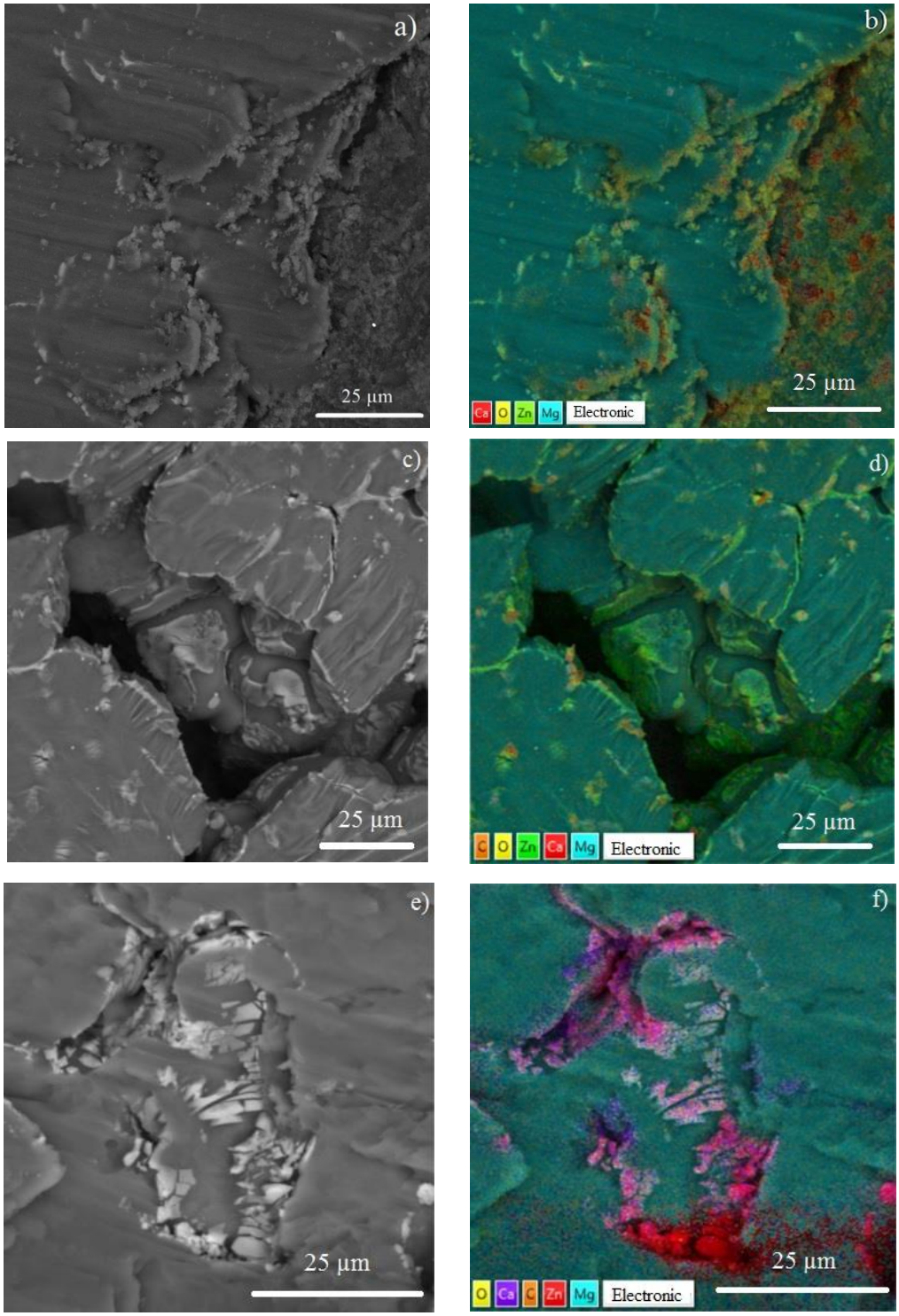

Figure 8. Results of element mapping of the fracture surface of magnesium alloys Mg–Ca–Zn reference (**a**,**b**), Mg–Ca–Zn–ND (**c**,**d**) and Mg–Ca–Zn US (**e**,**f**).

The fracture surface of the Mg–Ca–Z–ND alloy is sufficiently clean and exhibits spherical and elongated intermetallic inclusions after deformation and fracture (Figure 8c,d).

In addition, the carbon spectra can be observed, which confirms the presence of ND along the boundaries and in the magnesium grain. The fracture surface of the Mg–Ca–Zn US alloy exhibits traces of brittle fractured phases of calcium and zinc (Figure 8e,f), which apparently did not mix during casting to form $Ca_2Mg_6Zn_3$ and Mg_2Ca phases.

4. Conclusions

Ultrasonic melt treatment reduces the average grain size of the Mg–Ca–Zn alloy from 180 to 110 μm. The introduction of diamond nanoparticles without ultrasonic treatment reduces the average grain size of the Mg–Ca–Zn alloy from 190 to 80 μm, which is able to inhibit grain growth during solidification and is an effective grain refine for magnesium materials and also reduces the porosity of the alloy from 5 to 3 vol %.

The introduction of diamond nanoparticles increases the yield strength, ultimate strength and ductility of the Mg–Ca–Zn magnesium alloy from 66 to 75 MPa, from 294 to 332 MPa, and from 22 to 27%, respectively, due to a more uniform deformation of the magnesium matrix during compression. The increased yield strength of the Mg–Ca–Zn alloy can be due to the alloy grain refinement (Figure 4d,e) according to the Hall–Petch law, which directly affects an increase in the yield strength. The increased yield strength of the Mg–Ca–Zn alloy can due to the alloy grain refinement according to the Hall–Petch law, which directly affects an increase in the yield strength. A simultaneous increase in the tensile strength and ductility of the magnesium alloy attributed to a more uniform deformation of the material as a result of the ND introduction.

Further production optimization processing and study on the effect of the structure (including the effect of porosity and additives of non-metallic nanoparticles) on biocompatibility and rate of biodegradation should make it possible to determine the optimal phase composition and structure of medical magnesium alloys with improved physical and mechanical properties.

Author Contributions: Conceptualization, I.A.Z., A.P.K. and E.S.M.; methodology, I.A.Z. and E.S.M.; investigation, A.A. and A.N.M.; writing—original draft preparation, A.P.K. and I.A.Z.; writing—review and editing, A.P.K., E.S.M. and A.N.M.; project administration and funding acquisition, E.S.M.; supervision, A.B.V. All authors have read and agreed to the published version of the manuscript.

Funding: This work was carried out with financial support from the Ministry of Science and Higher Education of the Russian Federation (agreement no. 075-15-2021-1384).

Data Availability Statement: The data presented in this study are available in the article.

Acknowledgments: The research was done using equipment of Tomsk Regional Core Shared Research Facilities Centre of National Research Tomsk State University.

Conflicts of Interest: The authors declare no conflict of interest.

References

1. Wang, J.-L.; Xu, J.-K.; Hopkins, C.; Chow, D.H.-K.; Qin, L. Biodegradable Magnesium-Based Implants in Orthopedics—A General Review and Perspectives. *Adv. Sci.* **2020**, *7*, 1902443. [CrossRef] [PubMed]
2. Virtanen, S. Biodegradable Mg and Mg alloys: Corrosion and biocompatibility. *Mater. Sci. Eng. B* **2011**, *176*, 1600–1608. [CrossRef]
3. Xu, Z.; Smith, C.; Chen, S.; Sankar, J. Development and microstructural characterizations of Mg-Zn-Ca alloys for biomedical applications. *Mater. Sci. Eng. B* **2011**, *176*, 1660–1665. [CrossRef]
4. Huskins, E.L.; Cao, B.; Ramesh, K.T. Strengthening mechanisms in an Al-Mg alloy. *Mater. Sci. Eng. A* **2010**, *527*, 1292–1298. [CrossRef]
5. Lee, J.W.; Han, H.S.; Han, K.J.; Park, J.; Jeon, H.; Ok, M.R.; Seok, H.K.; Ahn, J.P.; Lee, K.E.; Lee, D.H.; et al. Long-term clinical study and multiscale analysis of in vivo biodegradation mechanism of Mg alloy. *Proc. Natl. Acad. Sci. USA* **2016**, *113*, 716–721. [CrossRef]
6. Castellani, C.; Lindtner, R.A.; Hausbrandt, P.; Tschegg, E.; Stanzl-Tschegg, S.E.; Zanoni, G.; Beck, S.; Weinberg, A.-M. Bone-implant interface strength and osseointegration: Biodegradable magnesium alloy versus standard titanium control. *Acta Biomater.* **2011**, *7*, 432–440. [CrossRef]
7. Xin, Y.; Hu, T.; Chu, P.K. In vitro studies of biomedical magnesium alloys in a simulated physiological environment: A review. *Acta Biomater.* **2011**, *7*, 1452–1459. [CrossRef] [PubMed]

8. Du, H.; Wei, Z.; Liu, X.; Zhang, E. Effects of Zn on the microstructure, mechanical property and bio-corrosion property of Mg-3Ca alloys for biomedical application. *Mater. Chem. Phys.* **2011**, *125*, 568–575. [CrossRef]
9. Staiger, M.P.; Pietak, A.M.; Huadmai, J.; Dias, G. Magnesium and its alloys as orthopedic biomaterials: A review. *Biomaterials* **2006**, *27*, 1728–1734. [CrossRef]
10. Prakasam, M.; Locs, J.; Salma-Ancane, K.; Loca, D.; Largeteau, A.; Berzina-Cimdina, L. Biodegradable materials and metallic implants—A review. *J. Funct. Biomater.* **2017**, *8*, 44. [CrossRef]
11. Pandey, A.; Awasthi, A.; Saxena, K.K. Metallic implants with properties and latest production techniques: A review. *Adv. Mater. Processing Technol.* **2020**, *6*, 405–440. [CrossRef]
12. Gilbert, J.L. Corrosion in the human body: Metallic implants in the complex body environment. *Corrosion* **2017**, *73*, 1478–1495. [CrossRef]
13. Datta, M.K.; Chou, D.-T.; Hong, D.; Saha, P.; Chung, S.J.; Lee, B.; Sirinterlikci, A.; Ramanathan, M.; Roy, A.; Kumta, P.N. Structure and thermal stability of biodegradable Mg-Zn-Ca based amorphous alloys synthesized by mechanical alloying. *Mater. Sci. Eng. B* **2011**, *176*, 1637–1643. [CrossRef]
14. Papillon, J.; Salero, P.; Mercier, F.; Fabrègue, D.; Maire, É. Compressive deformation behavior of dendritic Mg-Ca(-Zn) alloys at high temperature. *Mater. Sci. Eng. A* **2019**, *763*, 138180. [CrossRef]
15. Zhang, B.; Wang, Y.; Geng, L.; Lu, C. Effects of calcium on texture and mechanical properties of hot-extruded Mg-Zn-Ca alloys. *Mater. Sci. Eng. A* **2012**, *539*, 56–60. [CrossRef]
16. Bakhsheshi-Rad, H.R.; Idris, M.H.; Abdul-Kadir, M.R.; Ourdjini, A.; Medraj, M.; Daroonparvar, M.; Hamzah, E. Mechanical and biocorrosion properties of quaternary Mg-Ca-Mn-Zn alloys compared with binary Mg-Ca alloys. *Mater. Des.* **2014**, *53*, 283–292. [CrossRef]
17. Cai, C.; Song, R.; Wang, L.; Li, J. Effect of anodic T phase on surface micro-galvanic corrosion of biodegradable Mg-Zn-Zr-Nd alloys. *Appl. Surf. Sci.* **2018**, *462*, 243–254. [CrossRef]
18. Atrens, A.; Liu, M.; Zainal Abidin, N.I. Corrosion mechanism applicable to biodegradable magnesium implants. *Mater. Sci. Eng. B* **2011**, *176*, 1609–1636. [CrossRef]
19. Gnedenkov, S.V.; Sinebryukhov, S.L.; Mashtalyar, D.V.; Egorkin, V.S.; Sidorova, M.V.; Gnedenkov, A.S. Composite polymer-containing protective coatings on magnesium alloy MA8. *Corros. Sci.* **2014**, *85*, 52–59. [CrossRef]
20. Marchenko, E.; Baigonakova, G.; Yasenchuk, Y. Gradient crystalline coating on a biomedical TiNi alloy prepared by magnetron sputtering and annealing. *Vacuum* **2020**, *181*, 109652. [CrossRef]
21. Cui, X.J.; Ping, J.; Zhang, Y.J.; Jin, Y.Z.; Zhang, G.A. Structure and properties of newly designed MAO/TiN coating on AZ31B Mg alloy. *Surf. Coat. Technol.* **2017**, *328*, 319–325. [CrossRef]
22. Malaki, M.; Xu, W.; Kasar, A.K.; Menezes, P.L.; Dieringa, H.; Varma, R.S.; Gupta, M. Advanced Metal Matrix Nanocomposites. *Metals* **2019**, *9*, 330. [CrossRef]
23. Sharma, S.; Handa, A.; Singh, S.S.; Verma, D. Influence of tool rotation speeds on mechanical and morphological properties of friction stir processed nano hybrid composite of MWCNT-Graphene-AZ31 magnesium. *J. Magnes. Alloy.* **2019**, *7*, 487–500. [CrossRef]
24. Dinaharan, I.; Vettivel, S.C.; Balakrishnan, M.; Akinlabi, E.T. Influence of processing route on microstructure and wear resistance of fly ash reinforced AZ31 magnesium matrix composites. *J. Magnes. Alloy.* **2019**, *7*, 155–165. [CrossRef]
25. Zhang, Q.; Mochalin, V.N.; Neitzel, I.; Knoke, I.Y.; Han, J.; Klug, C.A.; Zhou, J.G.; Lelkes, P.I.; Gogotsi, Y. Fluorescent PLLA-nanodiamond composites for bone tissue engineering. *Biomaterials* **2011**, *32*, 87–94. [CrossRef]
26. Schrand, A.M.; Huang, H.; Carlson, C.; Schlager, J.J.; Ōsawa, E.; Hussain, S.M.; Dai, L. Are diamond nanoparticles cytotoxic? *J. Phys. Chem. B* **2007**, *111*, 2–7. [CrossRef] [PubMed]
27. Schrand, A.M.; Hens, S.A.C.; Shenderova, O.A. Nanodiamond particles: Properties and perspectives for bioapplications. *Crit. Rev. Solid State Mater. Sci.* **2009**, *34*, 18–74. [CrossRef]
28. Yuan, Y.; Wang, X.; Jia, G.; Liu, J.H.; Wang, T.; Gu, Y.; Yang, S.T.; Zhen, S.; Wang, H.; Liu, Y. Pulmonary toxicity and translocation of nanodiamonds in mice. *Diam. Relat. Mater.* **2010**, *19*, 291–299. [CrossRef]
29. Mohan, N.; Chen, C.S.; Hsieh, H.H.; Wu, Y.C.; Chang, H.C. In vivo imaging and toxicity assessments of fluorescent nanodiamonds in caenorhabditis elegans. *Nano Lett.* **2010**, *10*, 3692–3699. [CrossRef]
30. Watanabe, Y.; Sugiura, T.; Sato, H.; Tsuge, H. Fabrication of Al-based composites by centrifugal mixed-powder method and their application for grinding wheels. *J. Mater. Eng. Perform.* **2019**, *28*, 3852–3863. [CrossRef]
31. Huang, S.J.; Ali, A.N. Experimental investigations of effects of SiC contents and severe plastic deformation on the microstructure and mechanical properties of SiCp/AZ61 magnesium metal matrix composites. *J. Mater. Processing Technol.* **2019**, *272*, 28–39. [CrossRef]
32. Uozumi, H.; Kobayashi, K.; Nakanishi, K.; Matsunaga, T.; Shinozaki, K.; Sakamoto, H.; Tsukada, T.; Masuda, C.; Yoshida, M. Fabrication process of carbon nanotube/light metal matrix composites by squeeze casting. *Mater. Sci. Eng. A* **2008**, *495*, 282–287. [CrossRef]
33. Shakil, A.; Singh, S.K.; Rajak, B.; Gautam, R.K.; Rao, U.S. In situ infiltration synthesis and characterization of magnesium metal matrix composite. *Mater. Today Proc.* **2020**, *21*, 1223–1228. [CrossRef]
34. Purohit, R.; Dewang, Y.; Rana, R.S.; Koli, D.; Dwivedi, S. Fabrication of magnesium matrix composites using powder metallurgy process and testing of properties. *Mater. Today Proc.* **2018**, *5*, 6009–6017. [CrossRef]

35. Dieringa, H.; Hort, N. Magnesium-based metal matrix nanocomposites—Processing and properties. In *TMS Annual Meeting & Exhibition*; Springer: Cham, Switzerland, 2018; pp. 679–691. [CrossRef]
36. Yao, C.; Wang, Z.; Tay, S.L.; Zhu, T.; Gao, W. Effects of Mg on microstructure and corrosion properties of Zn–Mg alloy. *J. Alloys Compd.* **2014**, *602*, 101–107. [CrossRef]
37. Khrustalyov, A.P.; Kozulin, A.A.; Zhukov, I.A.; Khmeleva, M.G.; Vorozhtsov, A.B.; Eskin, D.; Chankitmunkong, S.; Platov, V.V.; Vasilyev, S.V. Influence of Titanium Diboride Particle Size on Structure and Mechanical Properties of an Al-Mg Alloy. *Metals* **2019**, *9*, 1030. [CrossRef]
38. Gromov, A.A.; Vorozhtsov, S.A.; Komarov, V.F.; Sakovich, G.V.; Pautova, Y.I.; Offermann, M. Ageing of nanodiamond powder: Physical characterization of the material. *Mater. Lett.* **2013**, *91*, 198–201. [CrossRef]
39. Vorozhtsov, S.; Vorozhtsov, A.; Kudryashova, O.; Zhukov, I.; Promakhov, V. Structural and mechanical properties of aluminium-based composites processed by explosive compaction. *Powder Technol.* **2017**, *313*, 251–259. [CrossRef]
40. Vorozhtsov, S.; Minkov, L.; Dammer, V.; Khrustalyov, A.; Zhukov, I.; Promakhov, V.; Khmeleva, M. Ex situ introduction and distribution of nonmetallic particles in aluminum melt: Modeling and experiment. *JOM* **2017**, *69*, 2653–2657. [CrossRef]
41. Zeka, B.; Markoli, B.; Mrvar, P.; Medved, J.; Petrič, M. Suitability of moulding materials for Al-Li alloy casting. *Mater. Technol.* **2021**, *55*, 311–316. [CrossRef]
42. Vorozhtsov, S.A.; Khrustalyov, A.P.; Eskin, D.G.; Kulkov, S.N.; Alba-Baena, N. The physical-mechanical and electrical properties of cast aluminum-based alloys reinforced with diamond nanoparticles. *Russ. Phys. J.* **2015**, *57*, 1485–1490. [CrossRef]
43. Rud, A.D.; Lakhnik, A.M.; Ivanchenko, V.G.; Uvarov, V.N.; Shkola, A.A.; Dekhtyarenko, V.A.; Ivaschuk, L.I.; Kuskova, N.I. Hydrogen storage of the Mg–C composites. *Int. J. Hydrogen Energy* **2008**, *33*, 1310–1316. [CrossRef]
44. Cao, H.; Huang, M.; Wang, C.; Long, S.; Zha, J.; You, G. Research status and prospects of melt refining and purification technology of magnesium alloys. *J. Magnes. Alloys* **2019**, *7*, 370–380. [CrossRef]
45. Ma, H.; Wang, J.; Wang, H.; Dong, N.; Zhang, J.; Jin, P.; Peng, Y. Influence of nano-diamond content on the microstructure, mechanical and thermal properties of the ZK60 composites. *J. Magnes. Alloys* **2021**. [CrossRef]
46. Zuo, Y.B.; Fu, X.; Mou, D.; Zhu, Q.F.; Li, L.; Cui, J.Z. Study on the role of Ca in the grain refinement of Mg–Ca binary alloys. *Mater. Res. Innov.* **2015**, *19*, 94–97. [CrossRef]
47. Shuai, S.; Guo, E.; Zheng, Q.; Wang, M.; Jing, T. Characterisation of three-dimensional dendritic morphology and orientation selection of α-Mg in Mg–Ca alloy using synchrotron X-ray tomography. *Mater. Charact.* **2016**, *111*, 170–176. [CrossRef]
48. Vostrý, P.; Stulíková, I.; Smola, B.; Riehemann, W.; Mordike, B.L. Structure and stability of microcrystalline Mg-Ca alloy. *Mater. Sci. Eng. A* **1991**, *137*, 87–92. [CrossRef]
49. Massalski, T.B.; Murray, J.L.; Bennett, L.H.; Baker, H. The Fe-Mo (Iron-Molybdenum) system. *Bin. Alloy Phase Diagr.* **1986**, *1–2*, 1079–1080.
50. Hansen, M.; Anderko, K. *Constitution of Binary Alloys*; McGraw-Hill: New York, NY, USA, 1958.
51. Bamberger, M.; Levi, G.; Vander Sande, J.B. Precipitation hardening in Mg-Ca-Zn alloys. *Metall. Mater. Trans. A* **2006**, *37*, 481–487. [CrossRef]
52. Du, Y.; Zheng, M.; Jiang, B. Microstructure modification and resultant mechanical properties of Mg-6Zn-1.5 Ca (wt%) alloy through hot extrusion. *J. Mater. Res.* **2018**, *33*, 1003–1010. [CrossRef]
53. Yan, L.; Zhou, J.; Sun, Z.; Yang, M.; Ma, L. Microstructure and bio-corrosion behaviour of Mg-5Zn-0.5Ca -xSr alloys as potential biodegradable implant materials. *Mater. Res. Express* **2018**, *5*, 045401. [CrossRef]
54. Kubásek, J.; Vojtěch, D. Structural characteristics and corrosion behavior of biodegradable Mg–Zn, Mg–Zn–Gd alloys. *J. Mater. Sci. Mater. Med.* **2013**, *24*, 1615–1626. [CrossRef] [PubMed]
55. Naik, S.N.; Walley, S.M. The Hall-Petch and inverse Hall-Petch relations and the hardness of nanocrystalline metals. *J. Mater. Sci.* **2020**, *55*, 2661–2681. [CrossRef]
56. Garkushin, G.V.; Razorenov, S.V.; Krasnoveikin, V.A.; Kozulyn, A.A.; Skripnyak, V.A. Effect of structural factors on mechanical properties of the magnesium alloy Ma2-1 under quasi-static and high strain rate deformation conditions. *Phys. Solid State* **2015**, *57*, 337–343. [CrossRef]
57. Kozulyn, A.A.; Skripnyak, V.A.; Krasnoveikin, V.A.; Skripnyak, V.V.; Karavatskii, A.K. An Investigation of Physico-Mechanical Properties of Ultrafine-Grained Magnesium Alloys Subjected to Severe Plastic Deformation. *Russ. Phys. J.* **2015**, *57*, 1261–1267. [CrossRef]
58. Dieringa, H.; Katsarou, L.; Buzolin, R.; Szakács, G.; Horstmann, M.; Wolff, M.; Mendis, C.; Vorozhtsov, S.; StJohn, D. Ultrasound Assisted Casting of an AM60 Based Metal Matrix Nanocomposite, Its Properties, and Recyclability. *Metals* **2017**, *7*, 388. [CrossRef]
59. Khrustalyov, A.P.; Garkushin, G.V.; Zhukov, I.A.; Razorenov, S.V.; Vorozhtsov, A.B. Quasi-Static and Plate Impact Loading of Cast Magnesium Alloy ML5 Reinforced with Aluminum Nitride Nanoparticles. *Metals* **2019**, *9*, 715. [CrossRef]
60. Promakhov, V.V.; Khmeleva, M.G.; Zhukov, I.A.; Platov, V.V.; Khrustalyov, A.P.; Vorozhtsov, A.B. Influence of Vibration Treatment and Modification of A356 Aluminum Alloy on Its Structure and Mechanical Properties. *Metals* **2019**, *9*, 87. [CrossRef]
61. Belov, N.A. Effect of eutectic phases on the fracture behavior of high-strength castable aluminum alloys. *Met. Sci. Heat Treat.* **1995**, *37*, 237–242. [CrossRef]